



3D printed fiber optic faceplates by custom controlled fused deposition modeling

YE WANG,¹ JOHN GAWEDZINSKI,¹ MICHAL E. PAWLOWSKI,¹ AND TOMASZ S. TKACZYK^{1,2,*}

¹Rice University, Department of Bioengineering, 6100 Main Street, Houston, 77005, USA

²Rice University, Department of Electrical and Computer Engineering, 6100 Main Street, Houston, 77005, USA

*ttkaczyk@rice.edu

Abstract: A 3D printing technique for manufacturing air-clad coherent fiber optic faceplates is presented. The custom G-code programming is implemented on a fused deposition modeling (FDM) desktop printer to additively draw optical fibers using high-transparency thermoplastic filaments. The 3D printed faceplate consists of 20000 fibers and achieves spatial resolution 1.78 LP/mm. Transmission loss and crosstalk are characterized and compared among the faceplates printed from four kinds of transparent filaments as well as different faceplate thicknesses. The printing temperature is verified by testing the transmission of the faceplates printed under different temperatures. Compared with the conventional stack-and-draw fabrication, the FDM 3D printing technique simplifies the fabrication procedure. The ability to draw fibers with arbitrary organization, structure and overall shape provides additional degree of freedom to opto-mechanical design. Our results indicate a promising capability of 3D printing as the manufacturing technology for fiber optical devices.

© 2018 Optical Society of America under the terms of the [OSA Open Access Publishing Agreement](#)

OCIS codes: (060.2340) Fiber optics components; (130.5460) Polymer waveguides.

References and links

1. K. V. Wong and A. Hernandez, "A review of additive manufacturing," *ISRN Mech. Eng.* **2012**, 208760 (2012).
2. B. C. Gross, J. L. Erkal, S. Y. Lockwood, C. Chen, & D. M. Spence, "Evaluation of 3D printing and its potential impact on biotechnology and the chemical sciences," *Anal. Chem.* **2014**, 3240–3253 (2014).
3. L. G. Bracaglia, B. T. Smith, E. Watson, N. Arumugasaamy, A. G. Mikos, and J. P. Fisher, "3D printing for the design and fabrication of polymer-based gradient scaffolds," *Acta Biomater.* **56**, 3–13 (2017).
4. P. Tack, J. Victor, P. Gemmel, and L. Annemans, "3D-printing techniques in a medical setting: a systematic literature review," *Biomed. Eng. Online* **15**(1), 115 (2016).
5. I. Gibson, D. Rosen, and B. Stucker, *Additive manufacturing technologies: 3D printing, rapid prototyping, and direct digital manufacturing*. Springer, 2014. Chapter 19.
6. Z. Liu, M. Zhang, B. Bhandari, and Y. Wang, "3D printing: Printing precision and application in food sector," *Trends Food Sci. Technol.* **69**, 83–94 (2017).
7. J. Sun, Z. Peng, W. Zhou, J. Y. Fuh, G. S. Hong, and A. Chiu, "A review on 3D printing for customized food fabrication," *Procedia Manufacturing* **1**, 308–319 (2015).
8. F. C. Godoi, S. Prakash, and B. R. Bhandari, "3d printing technologies applied for food design: Status and prospects," *J. Food Eng.* **179**, 44–54 (2016).
9. Y. W. D. Tay, B. Panda, S. C. Paul, N. A. Noor Mohamed, M. J. Tan, and K. F. Leong, "3D printing trends in building and construction industry: a review," *Virtual Phys. Prototyp.* **12**, 1–16 (2017).
10. S. C. Joshi and A. A. Sheikh, "3D printing in aerospace and its long-term sustainability," *Virtual Phys. Prototyp.* **10**(4), 175–185 (2015).
11. P. G. McMenamin, M. R. Quayle, C. R. McHenry, and J. W. Adams, "The production of anatomical teaching resources using three-dimensional (3D) printing technology," *Anat. Sci. Educ.* **7**(6), 479–486 (2014).
12. M. P. Chae, W. M. Rozen, P. G. McMenamin, M. W. Findlay, R. T. Spychal, & D. J. Hunter-Smith, "Emerging applications of bedside 3D printing in plastic surgery," *Frontiers Surgery* **2**, 2-22 (2015).
13. C. W. Hull, "Apparatus for production of three-dimensional objects by stereolithography." U.S. Patent No. 4,575,330. 11 Mar. 1986.
14. P. Calvert, "Inkjet printing for materials and devices." *Chem. Mater.* **13**(10), 3299–3305 (2001).
15. Stratasys, "PolyJet Technology", <http://www.stratasys.com/3d-printers/technologies/polyjet-technology>.
16. J. J. Beaman and C. R. Deckard, "Selective laser sintering with assisted powder handling." U.S. Patent No. 4,938,816. 3 Jul. 1990.

17. C. W. Ziemian and P. M. Crown III, "Computer aided decision support for fused deposition modeling," *Rapid Prototyping J.* **7**(3), 138–147 (2001).
18. F. Baumann, and D. Roller, "Vision based error detection for 3D printing processes." MATEC web of conferences. Vol. **59**. EDP Sciences, 2016.
19. S. Thiele, K. Arzenbacher, T. Gissibl, H. Giessen, and A. M. Herkommer, "3D-printed eagle eye: Compound microlens system for foveated imaging," *Sci. Adv.* **3**(2), e1602655 (2017).
20. J. Gawedzinski, M. E. Pawlowski, and T. S. Tkaczyk, "Quantitative evaluation of performance of three-dimensional printed lenses," *Opt. Eng.* **56**(8), 084110 (2017).
21. P.-I. Dietrich, R. J. Harris, M. Blaicher, M. K. Corrigan, T. M. Morris, W. Freude, A. Quirrenbach, and C. Koos, "Printed freeform lens arrays on multi-core fibers for highly efficient coupling in astrophotonic systems," *Opt. Express* **25**(15), 18288–18295 (2017).
22. T. Du, N. Cameron, M. Timothy, D. Yee, N. Dudukovic, J. Destino, C. Zhu, E. Duoss, T. F. Baumann, T. Suratwala, J. E. Smay, and R. Dylla-Spears, "3D-Printed Transparent Glass," *Adv. Mater.* **29**(26), 1701181 (2017).
23. J. Luo, L. J. Gilbert, D. A. Bristow, R. G. Landers, J. T. Goldstein, A. M. Urbas, and E. C. Kinzel, "Additive manufacturing of glass for optical applications," *Proc. SPIE* **9738**, 97380Y (2016).
24. F. Kotz, K. Arnold, W. Bauer, D. Schild, N. Keller, K. Sachsenheimer, T. M. Nargang, C. Richter, D. Helmer, and B. E. Rapp, "Three-dimensional printing of transparent fused silica glass," *Nature* **544**(7650), 337–339 (2017).
25. S. J. Leigh, R. J. Bradley, C. P. Pursell, D. R. Billson, and D. A. Hutchins, "A simple, low-cost conductive composite material for 3D printing of electronic sensors," *PLoS One* **7**(11), e49365 (2012).
26. M. Nierenberger, S. Lecler, P. Pfeiffer, F. Geiskopf, M. Guilhem, and P. Renaud, "Additive manufacturing of a monolithic optical force sensor based on polarization modulation," *Appl. Opt.* **54**(22), 6912–6918 (2015).
27. H. H. Duc Nguyen, U. Hollenbach, U. Ostrzinski, K. Pfeiffer, S. Hengsbach, and J. Mohr, "Freeform three-dimensional embedded polymer waveguides enabled by external-diffusion assisted two-photon lithography," *Appl. Opt.* **55**(8), 1906–1912 (2016).
28. H. H. D. Nguyen, U. Hollenbach, S. Pfirrmann, U. Ostrzinski, K. Pfeiffer, S. Hengsbach, and J. Mohr, "Photo-structurable polymer for interlayer single-mode waveguide fabrication by femtosecond laser writing," *Opt. Mater.* **66**, 110–116 (2017).
29. K. Willis, E. Brockmeyer, S. Hudson, and I. Poupyrev, "Printed optics: 3D printing of embedded optical elements for interactive devices," in *Proceedings of the 25th Annual ACM Symposium on User Interface Software and Technology* (ACM, 2012).
30. T. Pereira, S. Rusinkiewicz, and W. Matusik, "Computational light routing: 3d printed optical fibers for sensing and display," *ACM Trans. Graph.* **33**(3), 24 (2014).
31. K. Cook, J. Canning, S. Leon-Saval, Z. Reid, M. A. Hossain, J. E. Comatti, Y. Luo, and G. D. Peng, "Air-structured optical fiber drawn from a 3D-printed preform," *Opt. Lett.* **40**(17), 3966–3969 (2015).
32. K. Cook, G. Balle, J. Canning, L. Chartier, T. Athanaze, M. A. Hossain, C. Han, J. E. Comatti, Y. Luo, and G. D. Peng, "Step-index optical fiber drawn from 3D printed preforms," *Opt. Lett.* **41**(19), 4554–4557 (2016).
33. J. Canning, M. A. Hossain, C. Han, L. Chartier, K. Cook, and T. Athanaze, "Drawing optical fibers from three-dimensional printers," *Opt. Lett.* **41**(23), 5551–5554 (2016).
34. Y. Wang, M. E. Pawlowski, and T. S. Tkaczyk, "High spatial sampling light-guide snapshot spectrometer," *Opt. Eng.* **56**(8), 081803 (2017).
35. N. Bedard and T. S. Tkaczyk, "Snapshot spectrally encoded fluorescence imaging through a fiber bundle," *J. Biomed. Opt.* **17**(8), 080508 (2012).
36. A. Bodkin, A. Sheinis, A. Norton, A. Daly, J. Roberts, C. Beaven, and S. J. Weinheimer, "Video-rate chemical identification and visualization with snapshot hyperspectral imaging," *Proc. SPIE* **8374**, 83740C (2012).
37. B. Khoobehi, K. Firm, E. Rodebeck, and S. Hay, "A new snapshot hyperspectral imaging system to image optic nerve head tissue," *Acta Ophthalmol.* **92**(3), e241 (2014).
38. J. Kriesel, G. Scriven, N. Gat, S. Nagaraj, P. Willson, and V. Swaminathan, "Snapshot hyperspectral fovea vision system," *Proc. SPIE* **8390**, 83900T (2012).
39. I. Ishida, T. Akamatsu, Z. Wang, Y. Sasaki, K. Takenaga, and S. Matsuo, "Possibility of stack and draw process as fabrication technology for multi-core fiber," in *Optical Fiber Communication Conference and Exposition and the National Fiber Optic Engineers Conference (OFC/NFOEC)* (IEEE, 2013).
40. Stratasys, "Fortus 900mc", <http://www.stratasys.com/3d-printers/fortus-900mc>.

1. Introduction

Three-dimensional (3-D) printing, also referred to as additive manufacturing or rapid prototyping, is a technique used to fabricate 3-D objects from digital design files [1]. Compared with conventional manufacturing technologies, 3D printing enables rapid one-step fabrication while significantly lowering the cost and the material waste. 3D printing also offers unrestricted design freedom for manufacturers. Given these advantages, 3D printing has experienced tremendous growth in recent years and found applications in various domains

such as biomedical [2–4], automotive [5], food [6–8], construction [9], aerospace [10], education [11], and even cosmetic industry [12].

Stereolithography (SLA) was one of the first invented and commercialized 3D printing techniques [13]. In SLA, a beam of ultraviolet (UV) laser scans and polymerizes the photo-curable resin layer by layer to build a 3-D object. A variation of SLA technique is the digital light processing (DLP) printing. In DLP, a whole layer of printed part is polymerized during a single exposure. SLA and DLP are both photo-polymerization-based printing techniques, which offer a high spatial resolution ($< 1 \mu\text{m}$ with two-photon polymerization), but necessitate photo-polymerizable resin as the printing material. Another class of technique is jet-based printing, including 3-D inkjet [14], PolyJet [15], and selective laser sintering (SLS) [16]. In 3-D inkjet printing, each layer is finished by depositing droplets of binding liquid onto a layer of evenly distributed powder to bind the solid particles. Similarly, in SLS, each layer of powder is sintered by a high power laser. PolyJet distributes and instantly UV-cures droplets of liquid photopolymer. Jet-based printing offers a broader choice of material including polymers, metal, ceramic, and even biomaterials. Achievable resolution depends on the particle size of the fused material and the diameter of the laser spot. Fused deposition modeling (FDM) [17] is another widely used printing technique. In FDM, layers are fabricated by melting thermoplastic materials in a heated print head, followed by the filament extrusion and deposition layer by layer. Besides thermoplastic materials, such as polycarbonate (PC), acrylonitrile butadiene styrene (ABS) and nylon, FDM can print metals and ceramics with the usage of binders. The binders are usually mixed with ceramic or metal powders and convert the material into a filament form which is compatible with the FDM printers [2]. The typical resolution of FDM printer is above $100 \mu\text{m}$, which is limited by the nozzle diameter. Multi-material printing can be easily realized using the multi-extruder FDM print head. Nowadays, compact-size FDM machines have become the most prevalent type of consumer-grade 3D printers [18].

While 3D printing has been a matured technology in a wide range of industries, the 3D printing of optical components has just emerged as a new area in recent years. Typical examples include optical lenses [19–22], glasses [22–24], optoelectronic sensors [25,26], waveguides [27,28], and optical fibers [29–33]. In various optical imaging applications, such as optical tapers, inverted image-guides and fiber-based imaging spectrometers [34–38], optical fibers with complex structure of routes play an important role in the image reformatting and transfer and thus enable number of new applications. Compared with the conventional fiber optic device manufacturing techniques, the 3D printing technique adds more freedom to fiber designs and shortens the development cycle. Previous attempts on 3D printing of optical fibers were for example presented in 2012, when a PolyJet printer and transparent resin were used to print 0.5mm diameter “light pipes” [29]. Multiple applications of printed light guiding components were proposed, including ones designed for display applications, illumination and some optimized for use as sensors [29]. A path-designing algorithm for arbitrary printing routes of optical fibers was developed subsequently [30]. In 2015, a technique of printing air structured single optical fibers using FDM was explored by Cook et al [31]. His team printed the preforms of air structured optical fiber on an FDM printer and then drew them in an oven under a vacuum. The same technique was also used to fabricate step-index optical fibers [32]. In a recent study by Canning et al. [33], the extrusion nozzles of desktop FDM printers were characterized to have consistent temperature distribution profiles, indicating the printers to be suitable as micro-furnaces for drawing fibers. Optical fibers made from ABS and polyethylene terephthalate glycol (PETG) have been successfully drawn from these FDM printers, with comparable light losses to standard optical fibers, implying their potential application on short distance communications [33].

In this paper, we focus on the capability of FDM 3D printing technique to manufacture fiber optic devices. Specifically, we print fiber optic faceplates with parallel straight fibers for direct image transfer. Fiber optic faceplate is a simple demonstration of 3D printing capability

of coherent fibers, and an entry to more complex fiber devices. Typical applications of faceplates include CRT/LCD displays, CCD/CMOS sensor coupling, X-ray imaging/blocking and image intensifiers. Conventionally, fiber optic faceplates are fabricated by the “stack-and-draw” process [39], in which optical fibers are assembled into a preform, then heated and drawn down to a desired diameter. Preforms are later arrayed together and drawn down again until requested design parameters are met, such as fibers core diameters, fibers density and faceplate dimensions. Compared with the conventional stack-and-draw fabrication, the FDM 3D printing technique shortens build time, enables higher design flexibility, and thus opens the possibility of a paradigm shift in fiber optic device manufacturing and design.

As a first attempt, an air-clad fiber optic faceplate (faceplates with air as the cladding between printed fiber cores) was fabricated using single material FDM printing. Custom G-code was implemented to control a desktop FDM printer. Coherent fiber optic faceplate with 20000 fibers and a resolution of 1.78 LP/mm was successfully printed. Four types of commercial transparent thermoplastic filament were tested: ColorFabb XT-clear, Taulman3D Tech-G, Taulman3D t-glase, and Ultimaker CPE + . The transmission efficiency and crosstalk were characterized and compared and one optimal filament was selected. The transmission efficiencies and crosstalk were also measured for different faceplate thicknesses. The transmission of 3D printed faceplates was compared to a commercial available polymer fiber optic faceplate. The impact of different printing temperatures on the faceplate transmission was also tested.

2. Methods

An Ultimaker 3 dual extrusion 3D printer with 0.4mm nozzle diameter was used for printing. The printer was chosen because of its fine nozzle size and convenient process-control software. The printer offers two different printing modes: the auto-slicing mode and the custom G-code mode, giving two different printing methods for the faceplate. The auto-slicing method includes designing the 3-D model of the faceplate as a Standard Template Library (STL) file and then generating the printing procedures using the commercial slicing software (Cura 2.6.2). The custom G-code method allows designing custom G-code programs to directly control the printer’s extrusion process. The direct control over the parameters, such as the print head route, velocity, extrusion rate and temperature, enables optimizing the 3D print job for the specific faceplate structure. Preliminary experiments using auto-slicing software resulted in pathway artifacts and thus the printing results were not as satisfactory. The rest of the paper describes the printing procedure and results based on the custom G-code printing method.

Matlab R2017a was used to generate G-code files where the coordinates of the print head were calculated based on the analytical model of a faceplate. Fig. illustrates custom designed printing procedure. Each individual fiber was printed in a single pass of the extruder’s rectilinear motion parallel to the x-axis. In order to keep fibers dimension constant across the faceplate, the print head speed and extrusion rate were kept constant. Every layer consisted of fibers with a fixed core-to-core distance, and was printed by the back-and-forth path within the x-y plane as indicated in Fig. 1(a) (the red solid line arrows represents the extruder’s movement with constant extrusion and the red dashed line arrows represents the extruder’s movement without extrusion). A y-axis shift with half of the fiber core-to-core distance was introduced between even and odd number layer fibers (see Fig. 1(b), the red solid line arrows represents the fibers printed in odd layers and the green dashed line arrows represents the even layers). This shift results in a square fiber alignment which is rotated 45° in the y-z plane (see Fig. 1(c)). Figure 2 shows the optical micrograph (obtained by Olympus SZ61) of the faceplate end surface (y-z plane). Due to the plasticity of the material (under high temperature), the fiber’s cross-section was deformed into flat upper and bottom surfaces by the force of gravity and the pressure between adjacent fiber layers. Therefore, introducing the y-axis shift helps minimize the contact between neighboring fibers. Along the z-axis, the

layer-to-layer distance (layer height) was set to be the same as the shift distance. Figure 1(d) shows the 3-D view of the printed fibers' structure in the faceplate.

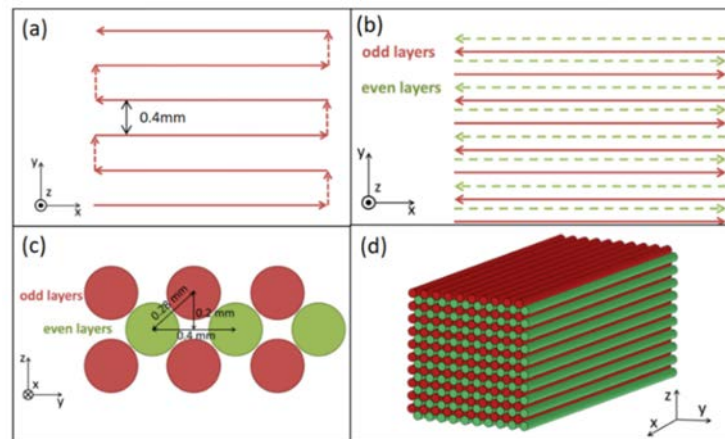


Fig. 1. Printing procedure of the fiber optic faceplate. (a) x-y plane top view of one single layer printing path; red solid line arrows: extruder's movement with constant extrusion; red dashed line arrows: extruder's movement with no extrusion (b) x-y plane top view of the extrusion path including multiple layers to illustrate the 0.2mm shift; solid line arrows: odd number layers extrusion; dashed line arrows: even number layers extrusion (c) y-z plane side view of the faceplate's fiber structure, with the red color representing odd number layers and green color representing even number layers (d) 3-D view of the designed fiber structure model

In this paper, the length of the printed fibers was first set as 10mm, giving a 10mm faceplate thickness. The faceplate was designed to have 200 layers with 100 parallel fibers in each layer, resulting in 20,000 fibers faceplate. The core-to-core distance of fibers within a layer was designed to be 0.4mm, which was driven by the extruder's diameter. The layer height and the odd-even layer shift were both 0.2mm (see Fig. (c)). Therefore, in the fibers' cross section plane (y-z plane), the faceplate had a dimension of 40mm x 40mm. Note that in this plane, the core-to-core distance of fibers along z-axis and y-axis was 0.4mm. However, each fiber was 0.28 mm from its nearest neighbor along the two directions which are 45 degree rotated from y-axis (see Fig. 1(c)). Therefore, the spatial resolution along these two 45 degree directions are both 0.28mm (1.78 lp/mm). By setting the extruder's moving speed to 2100 mm/min and the filament extrusion rate of 20.27 mm/min (filament diameter 2.85 mm), the diameter of the printed fiber was also controlled as 0.28 mm, to ensure a stable structure as well as minimize the contact-induced crosstalk.

To find an optimal printing material, faceplates were printed using four off-the-shelf commercial transparent filaments, including ColorFabb XT-clear, Taulman3D Tech-G, Taulman3D t-glase, and Ultimaker CPE + . All of the materials were printed with the temperature recommended by the manufacturer. Apart from the 10mm thick faceplate, faceplates with longer fiber lengths (30mm, 50mm, 70mm, and 90mm) were also printed for characterization purposes (see Results section).

To improve the light coupling efficiency, both ends of the faceplate (y-z plane) were sanded and polished using sand papers (3M P240 for 10 min, P400 for 10 min and P800 for 10 min) followed by the polishing on an automatic polisher (Ultra-Tec NanoPol Fiber Polishing system, 12 μm silicon carbide pads for 10 min and 1 μm silicon carbide pads for 10 min). Figure 2 shows the optical micrograph (obtained by Olympus SZ61) of the faceplate end surface (y-z plane). Due to the extruder pressure, the plasticity of the material (under high temperature) and the printing layer thickness, the cross section of individual fibers was rectangular.

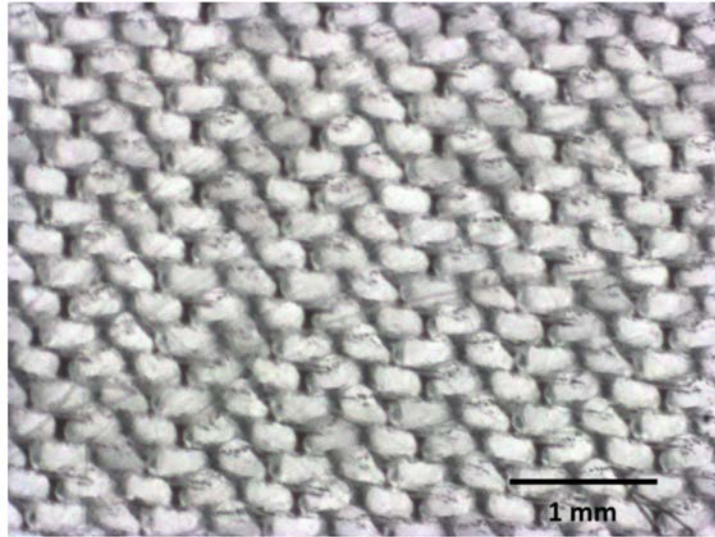


Fig. 2. Microscope (Olympus SZ61) image of the end surface (y-z plane) of the printed faceplate

3. Results

3.1 Off-the-shelf filament materials

To choose the optimal printing material for the faceplate, four commercially available transparent 2.85mm filaments which are compatible with the Ultimaker 3 printer were identified as candidate fiber optics materials: ColorFabb XT-clear, Taulman3D Tech-G, Taulman3D t-glase, and Ultimaker CPE + . For each material, a 10-mm thick faceplate was printed with the structure and procedure described in the Methods section. Optical transmission and contact-induced crosstalk of the four faceplates were characterized for performance comparison.

The optical transmission of the faceplates was characterized using the experimental system schematically presented in Fig. 3(a). A He-Ne laser (632.8 nm) served as a light source. An ND absorptive filter (Thorlabs NE30A, 25 mm, Optical Density 3.0) was placed directly after He-Ne laser to bring the beam intensity within the measurement range of the optical power meter. After passing through 10x achromatic expander (BE10M, Thorlabs), a 20 mm diameter laser beam was focused by a 10x/0.3 microscope objective (Olympus UPlanFL). The spot diameter in the image plane of the Olympus objective was measured to be 4.6 μm . The power of the spot was recorded by an optical power meter (Thorlabs S120C Standard Photodiode Power Sensor) and reported as the source power P_{source} . Then the spot was focused on the faceplate's input end plane (y-z plane) and coupled into one arbitrarily-selected fiber. The output power was measured at the output plane of the faceplate by the power meter, which was in direct contact with a tested faceplate as shown in Fig. 3(b). The measured output power was reported as P_{out} .

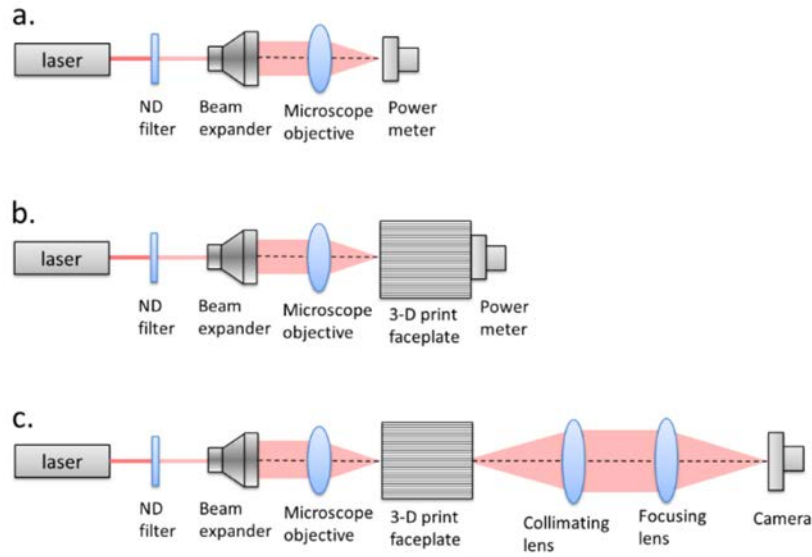


Fig. 3. Setup layout of transmission and crosstalk measurements. (a) Direct measurement of the input beam Power. (b) Transmission measurement of the 3D printed faceplate. (c) Crosstalk measurement by capturing the image of the output plane

The output power P_{out} for the four faceplates was measured under a same input power P_{source} . Due to the faceplate's air-clad structure in our design, contact-induced crosstalk between the adjacent fibers is inevitable. Therefore, P_{out} includes the output power from both the illuminated fiber and the crosstalk from adjacent fibers. Moreover, the crosstalk for different materials may differ because of their characteristics such as porosity and viscosity. To quantify the crosstalk and obtain the single fiber transmission, the image of the faceplate's output end was obtained by a collimating lens (Hasselblad 80 mm f/2.8, HC, Sweden, Gothenburg), a focusing lens (Sigma 85mm f/1.4 EX DG HSM) and a camera (Canon EOS 5D Mark II), as illustrated in Fig. 3(c). The pixel intensities recorded in the illuminated fiber's image was summed and denoted as S_i . The pixel intensities recorded within 4.75 mm radius of the illuminated fiber's center (the area of the power meter photodiode sensor used in Fig. 3(a)) were summed and denoted as S_n . The system crosstalk was defined in the equation below:

$$\text{Crosstalk} = \frac{S_n - S_i}{S_n} \times 100\%, \quad (1)$$

which represents the percentage of the light coupled into a certain fiber that scattered into the neighboring fibers at the output end while transmitting through the faceplate. For each of the five randomly-selected fibers, the transmission was calculated using following equation:

$$\text{Transmission} = \frac{P_{out}}{P_{source}} \times \frac{S_i}{S_n} \times 100\%, \quad (2)$$

which represents the percentage of the light coupled into a certain fiber at the input end that transmitted at the output end of the same fiber.

The transmission measurement of each faceplate was repeated for five arbitrary selected fibers. The mean value and standard deviation were calculated, as shown in Fig. 4(a). The XT-clear has the highest transmission of 50.08%, indicating the lowest loss among the four

candidate materials. The transmission for Tech-G, t-glase, and CPE + are comparable and all below 30% shown in Fig. 4(a).

Similar to the transmission characterization, the crosstalk measurement for each faceplate was repeated for five random-selected fibers, and the mean value among the five results was reported as the faceplate's crosstalk, together with the standard deviation shown in Fig. 4(b). According to the results, the XT-clear had the lowest crosstalk among the four tested materials (19.81%). The crosstalk for the t-glase and CPE + were comparable and around 30%. The Tech-G has the highest crosstalk among the four materials (42.53%).

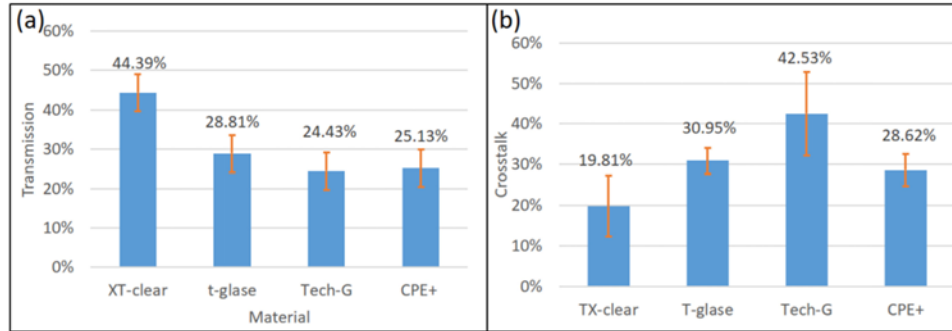


Fig. 4. Measured (a) transmission and (b) crosstalk of the faceplates printed in four materials including ColorFabb XT-clear, Taulman3D Tech-G, Taulman3D t-glase, and Ultimaker CPE + , with fiber length 10mm.

Combining the optical transmission and crosstalk characterization results, the ColorFabb XT-clear was found with the most satisfactory performance among the four candidate materials. Therefore, the XT-clear was chosen to print the faceplates as well as used in the further characterizations in the rest of the paper.

3.2 Faceplate performance in function of thickness

The fiber length in our 3D printed faceplates was designed as 10mm. However, faceplates with longer fiber lengths were printed to characterize their influence on the performance. Faceplates were printed with four longer arbitrary-selected fiber lengths: 30mm, 50mm, 70mm and 90mm. Their transmissions as well as crosstalk were characterized.

3.2.1 Transmission

We assume the transmission decays exponentially with the increased faceplate thickness, as described by Eq. (3), where P_{out} is the measured output power; L is the faceplate thickness and α indicates the attenuation coefficient. The P_{in} represents the actual input power coupled into the fiber. Due to the coupling loss on the air-fiber interface, P_{in} should be the measured source power P_{source} reduced by an unknown light coupling efficiency C , as described by Eq. (4).

$$P_{out} = P_{in} e^{-\alpha L} \quad (3)$$

$$P_{in} = CP_{source} \quad (4)$$

To quantify the transmission loss with the increased thickness, faceplates with five chosen thicknesses were tested: 10 mm, 30mm, 50mm, 70mm and 90mm. Similar to the material transmission characterization in Section 3.1, for each thickness of faceplate, one fiber was illuminated at the faceplate input end as described in Fig. 3(b). Then, transmission was measured and averaged among fiber random chosen fibers for each thickness respectively (asterisks in Fig. 5). The exponential decaying model described in Eqs. (2) and (4) was used

to interpolate the measured output powers (solid line in Fig. 5). According to the interpolation, the inferred light coupling efficiency C was 62.87%. The attenuation coefficient α was found to be 1.56 dB/cm, which is 3-5 times higher than the attenuation coefficient of the 3D printed single optical fibers reported in literature [33,34]. This may be because of the contact-induced crosstalk between neighboring fibers, which causes additional loss.

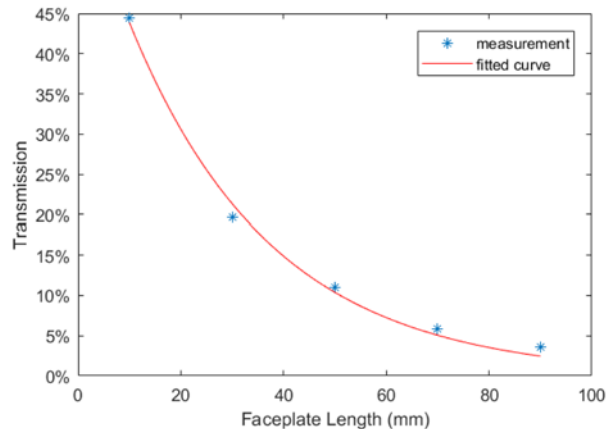


Fig. 5. Measured exponential decay of transmission with increased faceplate thickness. Material: ColorFabb XT-clear.

We also tested the transmission of a 5mm-thick commercial fiber optic faceplate (Paradigm Optics PA0370), and compared it with the faceplate printed with XT-clear. Under the same illumination, the transmission of the Paradigm Optics faceplate was measured as 75.98%. Based on the exponential decay model for the 3D printed faceplate, the interpolated output power shown in Fig. 5 at the length of 5mm was 52.51% as shown in Fig. 6. This result implied a comparable transmission between the 3D printed faceplate and commercial available fiber optic faceplates at short lengths.

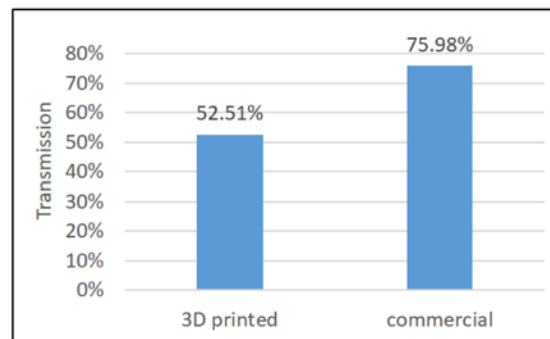


Fig. 6. Transmission comparison for the 3D printed ColorFabb XT-clear faceplate (interpolated at 5mm length) and the commercially available plastic faceplate (Paradigm Optics PA0370).

3.2.2 Crosstalk

We expect the contact-induced crosstalk increases with the increased fiber length. Using the optical system described in Section 3.1 and Fig. 3(c), output images as shown in Fig. 7 were obtained for the faceplate with three lengths: 10mm (a), 30mm (b), and 50mm (c). The white dashed circle on each image in Fig. 7 indicates the illuminated fiber. The crosstalk was calculated and averaged by 5 random-selected fibers in the same way described in Section 3.1, together with their standard deviations, as shown in Table 1 and Fig. 8. The crosstalk

increases significantly with increased fiber length. When the length reached 50mm, 80% of the light from the illuminated fiber scattered to the neighboring fibers. Therefore, for current air-clad printing technique, faceplates with short fiber lengths would be functional.

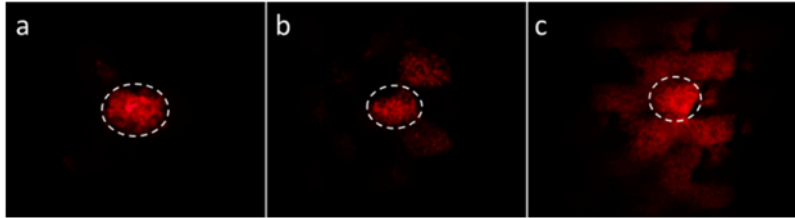


Fig. 7. The output end images for the 3D printed faceplate with three different lengths: (a) 10mm, (b) 30mm, and (c) 50mm. For each length, one fiber was illuminated at the input end, and the white dashed circles indicates the illuminated fiber at the output end. Material: ColorFabb XT-clear

Table 1. Crosstalk measurement for different faceplate thicknesses. Material: ColorFabb XT-clear

Length	10 mm	30 mm	50 mm
Crosstalk	19.81%	56.79%	80.74%
Standard deviation	7.46%	11.00%	4.10%

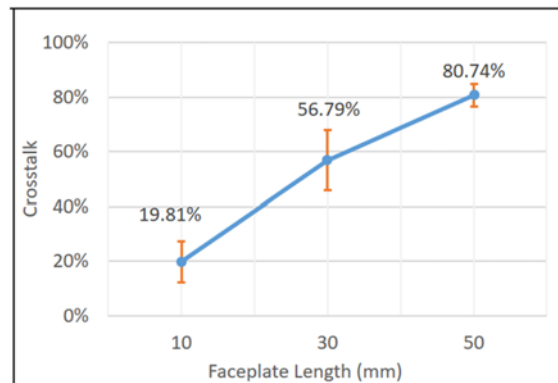


Fig. 8. Measured crosstalk of the faceplates for fiber lengths 10mm, 30mm and 50mm. Material: ColorFabb XT-clear

To potentially reduce the contact-induced crosstalk, an alternative printing pattern was designed by modifying the fiber alignment. As shown in Fig. 9(a), instead of printing the fibers all parallel in the original pattern (parallel pattern), we printed the even number layers along the direction perpendicular to the odd layers (perpendicular pattern). In this way, the even layers served as the interlayers to minimize the crosstalk, leaving the odd layers serving as the functional fibers.

Since the crosstalk becomes more evident for fiber lengths longer than 10mm, a 30mm-thick XT-clear faceplate in the perpendicular pattern was printed to better quantify the crosstalk reduction. The y-direction core-to-core distance between the fibers within one layer was kept the same as the parallel pattern (0.4mm) to guarantee sufficient separations. The layer height was also kept as 0.2mm. Therefore, each fiber in the perpendicular pattern was 0.4 mm from its nearest neighbors. The printing speed, temperature and extrusion rate were kept as the same as parallel pattern. The crosstalk of the perpendicular pattern faceplate was measured and compared to the 30mm-thick parallel pattern faceplate. As shown in Fig. 9(b), the crosstalk in the perpendicular pattern was 13.85%, which was around 25% of that

measured in the parallel pattern faceplate. Therefore, the perpendicular pattern reduced the contact-induced crosstalk.

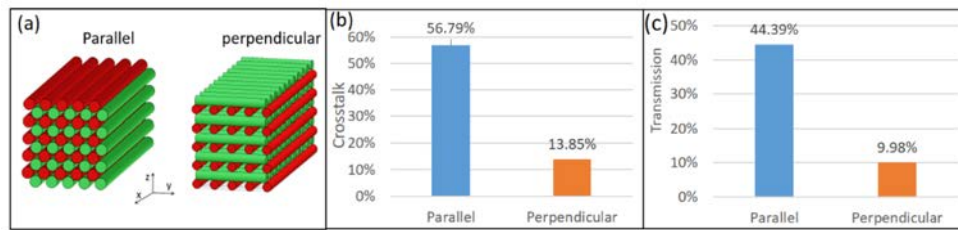


Fig. 9. Perpendicular printing pattern for crosstalk reduction. (a) 3-D view comparison of the parallel printing pattern and the perpendicular printing pattern. (b) Crosstalk comparison of the parallel and perpendicular printed faceplates. Thickness: 30mm; Material: ColorFabb XT-clear. (c) Measured transmission for the parallel and perpendicular printed faceplates. Thickness: 10mm; Material: ColorFabb XT-clear.

However, due to the absorption of the interlayers, the perpendicular pattern suffers from more transmission loss. A 10mm-thick perpendicular pattern faceplate was printed, whose transmission was measured in the same procedure as described in Section 3.1. The 10mm-thick parallel pattern faceplate was also measured under the same system. Figure 9(c) shows the measured transmission for both patterns. The perpendicular faceplate's output power was around 22% of the parallel faceplate. Moreover, in the perpendicular pattern, the distance between the nearest neighboring fibers are 0.4mm, which indicates a lower spatial resolution. Therefore, there's a trade-off between lower crosstalk and higher transmission as well as higher resolution when choosing between the two printing patterns.

3.3 Printing temperature and speed

The printing temperature for XT-clear was chosen to be 250 °C based on the manufacturer's recommendation. The printing speed was set to the default speed of commercial slicing software (Cura 2.6.2): 2100 mm/min. To investigate the impact of the printing temperature on the faceplate transmission, a series of 10 × 10 × 10mm faceplates were printed under five evenly spaced temperatures within the ± 20 °C interval around the manufacturer suggested temperature (220-270 °C). Note that for each printing temperature, the printing speed need to be optimized for a best transmission. Specifically, lower printing temperatures usually requires lower printing speeds. Therefore, for each temperature, we chose 5 different printing speeds which are within 10% - 200% interval around the original 2100 mm/min printing speed (210 – 4200 mm/min). Then the transmission of the faceplates were measured using the optical system described in section 3.1 and Fig. 3.

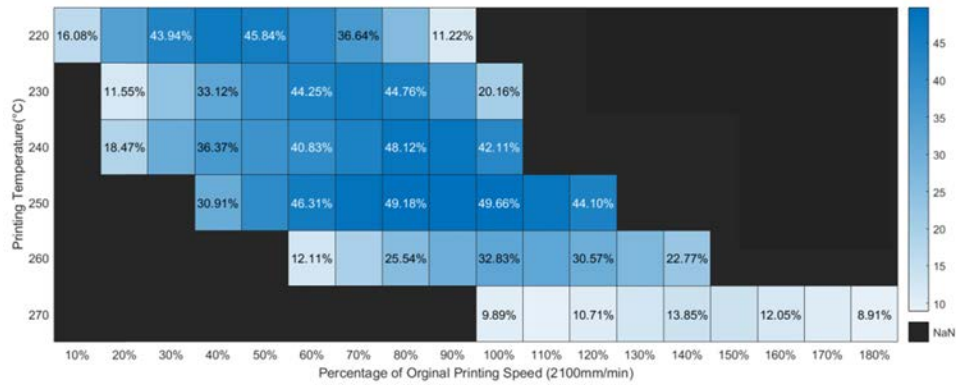


Fig. 10. (a) Measured transmission for the faceplates printed under different temperatures and different percentage of the original speed (2100mm/min). Cells with percentage value displayed are measured transmissions. Cells without displayed values are interpolated transmissions. Material: ColorFabb XT-clear

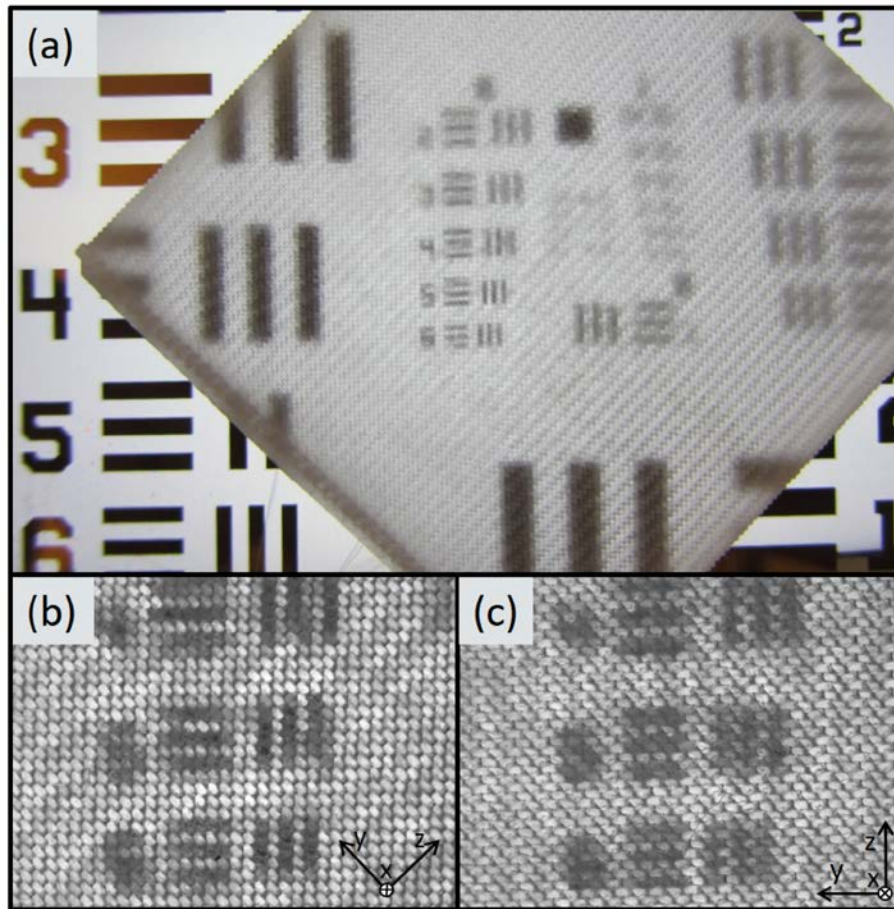


Fig. 11. (a) Image of the 1951 USAF resolution target in direct contact with the tested faceplate. The faceplate was rotated 45 degrees. USAF target was illuminated from behind using white LED (Thorlabs Mounted High Power LED MCWHL2). (b) Zoom-in area of (a) with the group 0, element 4, 5 and 6 under the microscope (Olympus SZ61). (c) The same area in (b) without rotating the faceplate 45 degrees, showing the y-axis and z-axis spatial resolution

Figure 10 shows a heat map of the measured transmission with both printing temperatures and speeds as variables. To better visualize the trend, for each temperature we interpolated four transmission values between the five measured transmission values. In Fig. 10, the cells with displayed percentage value are the measured transmissions, and cells without displayed values are interpolated transmissions. At the original printing speed (2100 mm/min), the XT-clear reached its maximum transmission at the temperature of 250 °C, which matches the temperature we chose for the faceplate printing. At lower printing temperature, the printing speed needs to be decreased for a relatively high transmission. For example, at 220 °C, the optimal printing speed needs to be around 50% of the original speed to reach a transmission comparable to 250 °C. Similarly, temperatures higher than 250 °C requires higher printing speed, but still suffer from significantly increased transmission loss. The average standard deviation of the transmission measurements in Fig. 10 is 6.8%.

3.4 Spatial resolution and imaging results

The spatial resolution of the fiber optic faceplate is limited by the fibers' core-to-core distance and core diameter. Note that both dimensions were kept 0.28mm along the 45 degrees rotated axis in the y-z plane as shown in Fig. 1(c). Therefore, the theoretical resolution of manufactured faceplate along this axis was 1.78 LP/mm, which corresponds to group 0, element 6 of the 1951 USAF resolution target. Figure 10(a) depicts one of the printed faceplates (material: XT-clear; thickness: 10mm) in direct contact with the 1951 USAF resolution target. Illumination was provided by a white LED (Thorlabs Mounted High Power LED MCWHL2) placed behind the resolution target. Note that when the faceplate was rotated 45 degrees, the components of group 0, element 6 are clearly distinguishable, which confirms that the face plate reached the theoretically predicted resolution. Figure 11(b) shows the zoom-in area with the group 0, element 4, 5 and 6 under the microscope (Olympus SZ61). Figure 11(c) shows the same area without rotating the faceplate 45 degrees, implying a lower spatial resolution along the y-axis and z-axis as shown in Fig. 1(c) corresponding to 1.25 LP/mm.

Figure 11 shows the faceplate's image guiding capability of macro features. Figure 11(a) displays the faceplates with fiber length 10mm guiding the image of a Rice University student identification card. In Fig. 12(b), a 30mm faceplate was used to image a laser-cut Rice mascot owl logo which was illuminated by a white-light LED (Thorlabs Mounted High Power LED MCWHL2). Figure 12(c) shows a 10mm thick faceplate placed at the image plane of a photographic objective (Sigma 85mm f/1.4 EX DG HSM) and capturing a Rice University campus view out of the window. In Fig. 12(d), three faceplates printed in XT-clear with various thickness: 10mm, 30mm and 50mm (from left to right) were placed on a paragraph of text to show the image guiding capability change with the increased fiber length.



Fig. 12. The image guiding capability of 3D printed faceplates for various macro features: (a) A Rice student identification card. (b) A laser-cut image mask of a Rice mascot owl logo at the input surface which is illuminated by a white-light LED. (c) A university campus view captured at the image plane of a photographic objective (Sigma 85mm f/1.4 EX DG HSM). (d) Image guiding capability comparison for various fiber lengths (from left to right: 10mm, 30mm, and 50mm)

4. Conclusions and discussions

In conclusion, the first high spatial density air-clad fiber optic faceplate fabricated by the FDM 3D printing technology has been demonstrated. The 3D printed faceplate consists of 20000 fibers and has a maximum spatial resolution of 1.78 LP/mm. The uniformity of the fiber's alignment and its consistency with the designed pattern has been presented. The optical transmission of the faceplates have been characterized and compared for various lengths, printing speed and for four different transparent 3D printing filaments. The ColorFabb XT-clear was measured to have the highest transmission as well as the lowest contact-induced crosstalk. Longer fiber lengths in the faceplate results in decreased transmission and increased crosstalk. The transmission of the 3D printed faceplate is comparable to the commercially available faceplates at short length. An alternative printing pattern was proposed with lower crosstalk but higher transmission loss and lower spatial resolution. The printing temperature was verified and the material's transparency was proved to be the maximal at the temperature chosen in our printing. Although the resolution is limited by the low-cost desktop FDM printer, this result demonstrates the capability of the 3D printing technique to manufacture fiber optical devices.

In the future, smaller fiber diameters and higher spatial resolution of the 3D printed faceplate will be realized by using FDM printers with smaller nozzles and higher control accuracy. Nowadays, the achievable resolution of the state-of-art FDM printers has reached below 100 μm [40], indicating the possibility of significant improvements. We will also introduce cladding to the faceplates to modify the numerical aperture of faceplates. This can be readily achieved by the FDM printer's ability to print with multiple materials.

Although limited by the nozzle size and accuracy of the low-cost desktop FDM printer, this work revealed the capability of 3D printing as a revolutionary fiber optic device manufacturing technique. Other than fiber optic faceplate, this technique can also be applied

to the fabrication of other fiber optic devices such as optical tapers, image-guides, etc. Compared with the traditional stack-and-draw fabrication technique, 3D printing enables an unlimited design freedom as well as shorter lead time. Therefore, an immediate advantage would be in the prototyping, where the test model of the design can be rapidly fabricated to examine the functionality and quality before putting into mass production. The fabrication of arbitrarily complex geometrical paths of fibers, such as inverted image guides or arbitrary surface shape displays, will no longer be as difficult and time-consuming as in traditional fabrication techniques. Fabrication of integrated functional modules can also be readily achieved by designing and printing multiple optical elements as one 3-D part. We envision a future world where more and more commercially available fiber optic devices are 3D printed. Moreover, a growing number of novel fiber optic devices will be inspired by the manufacturing revolution of 3D printing.

Funding

NASA ESTO 2016 ROSES A.42 Solicitation NNH16ZDA001N-IIP, award NNX17AD30G; National Cancer Institute of the National Institutes of Health (NIH) under Award Number R01CA186132.

Acknowledgments

We would like to acknowledge all the members in Tkaczyk lab for their helpful discussions and assistance. The content is solely the responsibility of the authors and does not necessarily represent the official views of NASA or NIH.

Disclosures

Dr. Tomasz Tkaczyk is the owner of the start-up, Attoris LLC., which focuses on commercializing hyperspectral instruments.